

# Impact of release dynamics of laser-irradiated polymer micropallets on the viability of selected adherent cells

Huan Ma<sup>1,2</sup>, Wael Mismar<sup>2,3</sup>, Yuli Wang<sup>4</sup>, Donald W. Small<sup>5</sup>,  
Mat Ras<sup>5</sup>, Nancy L. Allbritton<sup>4</sup>, Christopher E. Sims<sup>4</sup>  
and Vasan Venugopalan<sup>1,2,3,\*</sup>

<sup>1</sup>*Department of Chemical Engineering and Materials Science, University of California, 916 Engineering Tower, Irvine, CA 92697-2575, USA*

<sup>2</sup>*Laser Microbeam and Medical Program, Beckman Laser Institute and Medical Clinic, University of California, Irvine, CA 92697-1475, USA*

<sup>3</sup>*Department of Biomedical Engineering, University of California, Irvine, CA 92697-2715, USA*

<sup>4</sup>*Department of Chemistry, The University of North Carolina at Chapel Hill, Chapel Hill, NC 27599-3290, USA*

<sup>5</sup>*Lightworks Optics, 14242 Chambers Road, Tustin, CA 92780-6910, USA*

We use time-resolved interferometry, fluorescence assays and computational fluid dynamics (CFD) simulations to examine the viability of confluent adherent cell monolayers to selection via laser microbeam release of photoresist polymer micropallets. We demonstrate the importance of laser microbeam pulse energy and focal volume position relative to the glass–pallet interface in governing the threshold energies for pallet release as well as the pallet release dynamics. Measurements using time-resolved interferometry show that increases in laser pulse energy result in increasing pallet release velocities that can approach  $10 \text{ m s}^{-1}$  through aqueous media. CFD simulations reveal that the pallet motion results in cellular exposure to transient hydrodynamic shear stress amplitudes that can exceed 100 kPa on microsecond time-scales, and which produces reduced cell viability. Moreover, CFD simulation results show that the maximum shear stress on the pallet surface varies spatially, with the largest shear stresses occurring on the pallet periphery. Cell viability of confluent cell monolayers on the pallet surface confirms that the use of larger pulse energies results in increased rates of necrosis for those cells situated away from the pallet centre, while cells situated at the pallet centre remain viable. Nevertheless, experiments that examine the viability of these cell monolayers following pallet release show that proper choices for laser microbeam pulse energy and focal volume position lead to the routine achievement of cell viability in excess of 90 per cent. These laser microbeam parameters result in maximum pallet release velocities below  $6 \text{ m s}^{-1}$  and cellular exposure of transient hydrodynamic shear stresses below 20 kPa. Collectively, these results provide a mechanistic understanding that relates pallet release dynamics and associated transient shear stresses with subsequent cellular viability. This provides a quantitative, mechanistic basis for determining optimal operating conditions for laser microbeam-based pallet release systems for the isolation and selection of adherent cells.

**Keywords:** laser-induced forward transfer; laser catapulting; shear stress; plasma formation; laser ablation; iCell

## 1. INTRODUCTION

The procurement of single or groups of cells with specific characteristics is critical for many areas of biomedical research. While numerous strategies exist to separate and collect non-adherent cells, including limiting dilution, panning method, magnetic sorting and fluorescence-activated cell sorting [1], the options for

adherent cells are limited. Enzymatic or mechanical methods used to release the cells from their growth surface during suspension preparation or cell collection can result in the loss of cell viability and morphology, removal of cell surface markers, damage to cell membrane and alteration in cell physiology [2,3].

Laser microdissection (LMD) and laser pressure catapulting (LPC) developed in the 1990s is a rapid, non-contact method to isolate and select histological specimens as well as single and/or groups of cells

\*Author for correspondence (vvenugop@uci.edu).

[4–9]. The LMD/LPC technique is well-known and extensively documented in the literature [5,10]. Briefly, cellular or tissue samples are grown or mounted on a thin UV-absorbing polymer film, which is subsequently placed on a transparent substrate such as a microscope cover glass. The region of interest to be selected on the polymer film is identified through direct visualization, and dissected using a pulsed UV laser. The dissected sample is catapulted by a single laser pulse through a laser-induced forward transfer process known as LPC and collected by a cap that is wetted with culture medium. While the combination of LMD and LPC has been tremendously successful for the isolation and subsequent analysis of histological sections, the viability of live cellular samples acquired using these methods is adversely impacted owing to the damage through direct UV irradiation, heat transfer from the UV-irradiated polymer foil, mechanical disruption from the catapulting process and desiccation from removal of fluid overlying the sample during collection [6–8]. Moreover, in LPC, it is not sufficient to merely release the sample, the process must also impart sufficient momentum so that the sample is successfully transported through the air and into a collection receptacle that is positioned millimetres away from the target surface.

Over the last five years, the Allbritton group has developed a novel approach to isolate and select individual and/or groups of adherent cells from a mixed cell population using polymer micropallet arrays [11–13]. These arrays are fabricated on top of a glass substrate using photolithographic methods [14]. The top of the micropallets can be coated with collagen or fibronectin to facilitate adherent cell attachment and culture. The micropallets can be visualized under microscopic examination and subsequently released via delivery of a single-pulsed laser microbeam exposure focused near the interface of the micropallet and the glass substrate. Pallet release occurs on the microsecond timescale and is driven by a plasma-mediated ablation process initiated by the pulsed laser microbeam exposure [15].

Compared with LMD/LPC, the micropallet method employs visible laser radiation ( $\lambda = 532$  nm) to avoid UV damage to the cells. Moreover, the micropallet height is typically 30–50  $\mu\text{m}$  and much larger than the 2  $\mu\text{m}$  thick polymer foils used in LMD/LPC. This provides greater cellular isolation from the thermal effects and mechanical stresses produced by the laser/polymer interaction. In addition, once the cells are introduced, the micropallets are not exposed to air but are instead immersed in growth media during the entire selection, separation and collection procedure. Unlike other printing methods that use laser-based ejection, e.g. laser-induced forward transfer and laser-assisted bioprinting, the pallet release method has been used strictly for the isolation and separation of live adherent cells and there is no transfer of the cellular sample and underlying substrate to an ‘acceptor’ surface. These process characteristics have enabled the Allbritton group to obtain excellent (greater than 90%) cell viability and recultivation efficiency in their experiments [11–13]. The combined use of polymer microarrays for cell culture and pulsed laser microbeam

irradiation for release has been used successfully to isolate and select cells for subsequent recultivation based on criteria such as cellular morphology, fluorescence and gene expression for creating cell lines and rapid production of stable transfections [11,16]. Moreover, this approach has been applied successfully for the isolation, sorting and expansion of haematopoietic and embryonic stem cell colonies for further examination and for applications such as the creation of transgenic animals [17,18].

Nevertheless, several laser microbeam parameters must be adjusted to achieve consistent pallet release without loss of cell viability. The laser microbeam pulse energy should be sufficient to achieve consistent pallet release and yet be low enough to mitigate against cellular damage. Previous research in our group has determined that while the pulse energy necessary for pallet release is independent of laser pulse duration [15], it is quite sensitive to the axial location of the laser microbeam focal volume relative to the glass–pallet interface. This axial position of the laser microbeam focal volume affects the degree to which the cells are exposed to laser microbeam radiation, the pallet release dynamics and the subsequent cell viability. While the shock wave produced by the pallet release process is unlikely to cause cellular injury [19], the rapid motion of the pallet through the aqueous cell culture medium can subject the cells to significant hydrodynamic shear stresses. Previous studies have demonstrated that cellular exposure to large transient shear stresses (1–100 kPa) on the microsecond timescale initiated by pulsed laser microbeam irradiation is responsible for a variety of effects ranging from cell lysis, necrosis, detachment and transient membrane permeabilization [20–23].

In this paper, we report on experimental and computational studies that investigate the effect of laser microbeam pulse energy and focal volume location on the probability of pallet release, the pallet release dynamics, the cellular exposure to hydrodynamic shear stresses and subsequent cell viability. These studies are meant to: (i) provide a basis for the optimization of laser microbeam irradiation parameters for pallet release while preserving cell viability and (ii) identify the key physical characteristics of the pallet release process that governs the potential loss of cell viability. An understanding of the influence of the pallet release dynamics on the subsequent biological response will likely be instructive for the design and widespread adoption of micropallet release systems.

## 2. MATERIAL AND METHODS

### 2.1. *Pallet microarray fabrication*

We used arrays consisting of 21 560  $100 \times 100$   $\mu\text{m}$  square pallet elements with a thickness of 50  $\mu\text{m}$  and inter-pallet spacing of 20  $\mu\text{m}$ , as shown in figure 1. The pallets were fabricated using 1002F photoresist polymer on a 0.9 mm thick BK-7 glass support [14]. Focus alignment marks composed of titanium were present on the top surface of the BK-7 glass. Compared with the more widely used photoresist SU-8, 1002F

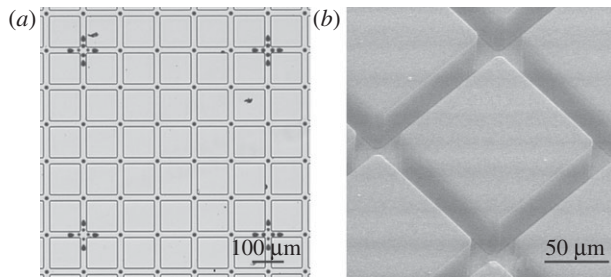


Figure 1. (a) Light and (b) electron microscopy of 1002F pallet arrays. The pallet elements are 50  $\mu\text{m}$  tall and have lateral dimensions of  $100 \times 100 \mu\text{m}$ . Adjacent pallet elements are separated by 20  $\mu\text{m}$  to form the array. Titanium markings deposited onto the underlying glass support and used for accurate focusing appear as black ‘dots’ adjacent to the corner of each pallet element in the light microscopy image.

has lower endogenous fluorescence for better visualization and imaging when using fluorescence-based cellular assays [24].

## 2.2. Measurement of threshold energy for pallet release

Figure 2 shows the experiment set-up used to measure the threshold laser microbeam energy necessary for the pallet release. We used a passively Q-switched frequency-doubled Nd:YAG microchip laser ( $\mu\text{Flare PQ Green 10-20}$ , InnoLight GmbH, Hannover, GERMANY) that provides 1 ns duration pulses at  $\lambda = 532 \text{ nm}$ . As shown, the laser beam is expanded and collimated by a beam expander consisting of a pair of spherical lenses. The combination of a half-wave ( $\lambda/2$ ) plate and polarizing beam splitter serves as a beam attenuator to adjust the laser pulse energy to the desired value. The maximum output pulse energy of the laser is approximately 20  $\mu\text{J}$ . We set the iris diameter to 8 mm to match the rear aperture of the microscope objective lens. The iris is overfilled by the laser beam to obtain the near-diffraction-limited focal spot size. The laser pulse energy is measured by an energy meter (EPM1000 with J5-09 sensor, Coherent Inc., Santa Clara, CA, USA). A flip mirror is used to select the optical path between the energy meter and the back port of the inverted microscope (IX-81, Olympus America, Center Valley, PA, USA). Once the laser pulse enters the microscope, it is reflected by a dichroic beam splitter (ZT532NBDC, Chroma Technology Corp., Bellows Falls, VT, USA) and then focused by a  $20\times$ , 0.45 NA microscope objective lens (LUCPLFLN, Olympus America) into the pallet. Under these focusing conditions, a pulse energy of 1  $\mu\text{J}$  results in a radiant exposure of  $0.61 \text{ J mm}^2$  in the focal plane. The position of the microbeam focal volume can be adjusted by raising or lowering the objective lens using the automated microscope stepper motor. The position of the microbeam focal volume is measured relative to the image plane corresponding to the interface between the BK-7 glass support and the polymer pallet. The precision of this placement is less than the Rayleigh range and corresponds to approximately  $\pm 1 \mu\text{m}$  for the 0.45 NA objective. Owing to refraction, the height of the

focal volume with respect to the interface between the polymer pallet and the glass slide  $h'$  is  $n_p$  times the objective lens travel distance  $h$ , where  $n_p$  is the refractive index of the polymer pallet. Positive  $h$  and  $h'$  values represent cases where the focal volume is placed within the polymer pallet whereas negative values denote cases where the focal volume is placed within the BK-7 glass support.

## 2.3. Measurement of pallet release dynamics

The dynamics of the early stages of pallet release are measured using a modified Mach-Zehnder time-resolved heterodyne interferometer as depicted in figure 3a. This measurement approach has been demonstrated to provide nanosecond time resolution and sub-nanometre displacement sensitivity [25–28]. As shown in figure 3, an acousto-optic modulator (AOM) (ATM-1101A1, IntraAction Corp., Bellwood, IL, USA) operated by a radio-frequency driver (VFE, IntraAction Corp.) is used to split a  $\lambda = 633 \text{ nm}$  stabilized HeNe laser (32734, Research Electro-Optics, Inc. Boulder, CO, USA) beam and shift the frequency of the diffracted beam by 110 MHz. The frequency-shifted beam serves as the reference beam of the interferometer while the unshifted beam serves as the probe beam and is focused on the top surface of a pallet element by a condenser lens. The polarization of the unshifted laser beam is manipulated by a quarter-wave plate to maximize the signal reflected back to the interferometer. To increase the light collection efficiency, a  $20 \times 0.50 \text{ NA}$  water immersion objective lens (HCX APO L, Leica Microsystems GmbH, Wetzlar, GERMANY) is used instead of the standard condenser lens. The reference beam is combined with the probe beam at the non-polarizing beam splitter. The half-wave plate is used to align the polarizations of two beams along the same direction so that the two beams can interfere with each other. The two output beams from the non-polarizing beam splitter are sent to a balanced detector [29] consisting of two 500 MHz photodiodes (S5972, Hamamatsu Photonics, Hamamatsu City, JAPAN) and accompanying circuit, after being filtered by two  $\lambda = 633 \text{ nm}$  band pass filters (10 nm FWHM). The mixed signal is amplified by a low-noise amplifier (ZFL500-LN, Mini-Circuits, Brooklyn, NY, USA) and recorded by a 500 MHz digital oscilloscope (WaveRunner 6051A, LeCroy Corporation, Chestnut Ridge, NY, USA). To enhance the probe signal quality in these experiments, we applied a thin dielectric reflective coating to the exposed pallet surface and performed these measurements without cells cultured on the pallet surface. The absence of the HeLa cell monolayer should have a negligible impact on the pallet dynamics as the thickness of the HeLa cell body is less than 5  $\mu\text{m}$ , which would contribute less than 10 per cent to the overall mass [30].

The displacement of the sample surface  $z(t)$  is proportional to the instantaneous phase difference between the interferometer signal  $\Phi_{\text{INT}}(t)$  and the AOM driving signal  $\Phi_{\text{AOM}}(t)$  [25]:

$$z(t) = \frac{\lambda[\Phi_{\text{INT}}(t) - \Phi_{\text{AOM}}(t)]}{4\pi}, \quad (2.1)$$

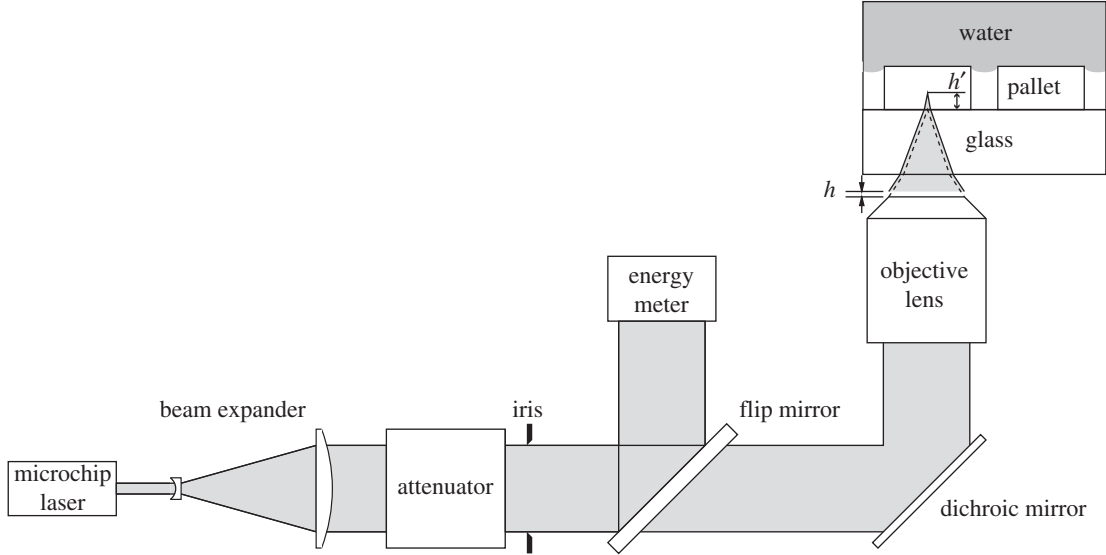


Figure 2. Schematic of pallet release energy threshold measurement.

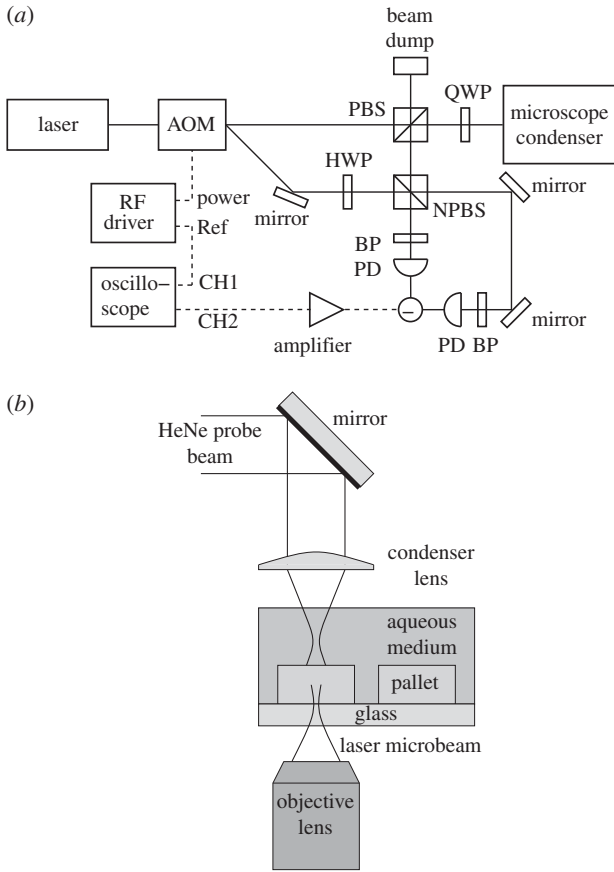


Figure 3. Schematic of the time-resolved heterodyne interferometer. AOM, acousto-optic modulator; PBS, polarizing beam splitter; QWP, quarter-wave plate; HWP, half-wave plate; NPBS, non-polarizing beam splitter; BP, band pass filter; PD, photodiode; power, power output of RF driver (high power); Ref, reference output of RF driver (low power); CH1, channel 1 of oscilloscope and CH2, channel 2 of oscilloscope.

where  $\lambda$  is the wavelength of the HeNe laser in water (or cell culture media). The time-resolved phases  $\Phi_{\text{INT}}(t)$  and  $\Phi_{\text{AOM}}(t)$  can be obtained by applying the Hilbert transform to the detected interferometer

signal  $I_{\text{INT}}(t)$  and the AOM driving signal  $I_{\text{AOM}}(t)$ , respectively:

$$\Phi_{\text{INT,AOM}} = \arctan \left\{ \frac{\mathcal{H}[I_{\text{INT,AOM}}(t)]}{I_{\text{INT,AOM}}(t)} \right\}, \quad (2.2)$$

where  $\mathcal{H}$  denotes the Hilbert transform. To reduce noise, a 160 MHz FWHM digital band pass filter centred at 110 MHz was applied to the raw interferometer signal before data processing. With this time-resolved displacement, the velocity and acceleration are obtained by differentiation. Interferometric measurements of pallet release dynamics were performed for laser microbeam pulse energies  $E_p = 2.5, 3.0$  and  $3.5 \mu\text{J}$ , and axial focal volume heights  $h = 2, 6$  and  $10 \mu\text{m}$ .

#### 2.4. Pallet preparation and cell culture

To prepare the pallet arrays fabricated in §2.1 for cell culture, we formed a hydrophobic perfluoroalkylsilane layer onto the 1002F micropallet surface. The silanization process allows the air to be trapped between the pallets and results in heterogeneous Cassie–Baxter wetting of the hydrophobic surface of the pallet array [31]. This restricts cell attachment only to the top surface of the pallet elements. The array was placed into a desiccator along with a Petri dish containing  $100 \mu\text{l}$  of (heptadecafluoro-1,1,2,2-tetrahydrodecyl) trichlorosilane. The desiccator was attached to an oil-free vacuum pump for 1 min and maintained under vacuum over 16 h at room temperature. The array alone was then placed under high vacuum for 2 h to remove any unreacted silane.

The micropallet array was sterilized with ethanol and dried in a tissue culture hood. The top surface of the array was coated with  $25 \mu\text{g ml}$  of fibronectin for 2 h in an incubator to enhance cell adhesion. The array was then rinsed five times with phosphate-buffered saline. HeLa cells were cultured onto the micropallets in Dulbecco's modified Eagle's medium (DMEM) supplemented with 10 per cent foetal bovine

serum (FBS), L-glutamine ( $584 \mu\text{g ml}^{-1}$ ) and 1 per cent streptomycin at  $37^\circ\text{C}$  and 5 per cent  $\text{CO}_2$  within the incubator. The micropallets were seeded initially with HeLa cells at low density (approx. 1 cell per pallet element) and held in culture for 4–5 days for the monolayer to be established.

### 2.5. Cell viability and recultivation following pallet release

Immediately prior to the experiment, the micropallets, now covered with a monolayer of cells on their top surface, were rinsed with fresh media to wash away any dead cells. The confluent micropallets were co-stained with 4 ml solution of  $2 \mu\text{M}$  calcein acetomethoxy (AM) containing  $4 \mu\text{g}$  of Hoechst 33342 stain (Invitrogen Corporation, Carlsbad, CA, USA) for 30 min in the tissue culture hood. Hoechst 33342 is a DNA-binding fluorescent stain and was used to facilitate cell counting. Calcein AM is a cell-permeant molecule that is used as a cell-viability indicator. Upon entering a live cell, calcein AM is acted on by cellular esterases to cleave the AM group where upon it becomes fluorescent and trapped within the cell. Dead cells lack active esterases and thus only live cells are fluorescent. Fresh DMEM was then added to the micropallet until fluorescence imaging. This co-staining allows confirmation and proper selection of pallet elements that contain a fully viable and confluent HeLa cell monolayer. Prior to release, cultured micropallets were capped onto an imaging dish that was completely filled with DMEM and supplemented with 10 per cent foetal bovine serum (FBS), L-glutamine ( $584 \mu\text{g ml}^{-1}$ ) and 1 per cent streptomycin. In addition, 2 ml of conditioned medium taken from sub-confluent cultured HeLa cells was added to the DMEM solution [12]. The complete filling of the dish ensured that the micropallet array was fully submerged with media.

A prototype pallet release apparatus (iCell, Lightworks Optics, Tustin, CA, USA) was used to release pallets in the cell viability experiment [32]. The apparatus uses a passively Q-switched solid-state diode-pumped laser ( $\mu\text{Flare PQ Green 10-20}$ , InnoLight GmbH, Hannover, GERMANY) that emits  $\lambda = 532 \text{ nm}$  pulses of 1 ns duration for the pallet irradiation. The laser beam was directed into an upright microscope (IX-51, Olympus America) and focused into the pallet at a fixed focal volume position  $h = 6 \mu\text{m}$  using a  $20\times$ , 0.45 NA microscope objective (LUCPLFLN, Olympus America) using pulse energies of 2.5, 3.0 or  $3.5 \mu\text{J}$ . The glass–pallet interface was identified by bringing into focus alignment marks that were present on the top surface of the glass. In this way, the location of the glass–pallet interface was determined for each pallet prior to laser microbeam delivery. For each pulse energy examined, a minimum of 20 pallet elements were released and all of the released pallet elements were collected for analysis. In these experiments, each pallet element typically had 8–12 ‘resident’ cells. Cell counts and viability were subsequently assessed 60–90 min following pallet release using fluorescence microscopy on an inverted microscope (IX-81, Olympus America). In forming the digital images, we encoded the calcein AM fluorescence in the green channel and the

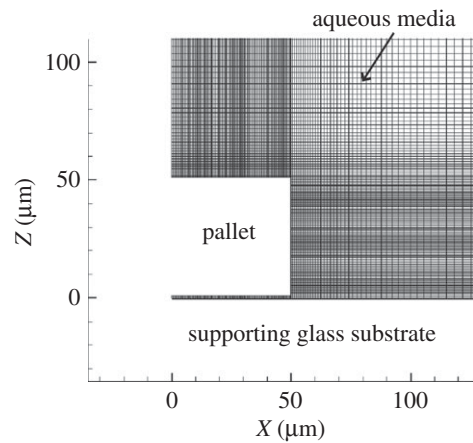


Figure 4. Central region of the dynamic mesh used for the CFD simulation. The underlying glass support occupies the region  $Z \leq 0$  while the fluid is present in regions occupied by the mesh. The overall computation domain is  $1.5 \times 1.5 \text{ mm}$ . The mesh resolution is  $1 \mu\text{m}$  in regions immediately adjacent to the pallet and increases gradually to  $10 \mu\text{m}$  at the outer boundaries of the computational domain.

Hoechst 33342 fluorescence in the red channel. This results in viable cells taking on an appearance where the nucleus is reddish-orange and the cytoplasm is green. For dead cells, the non-fluorescent calcein AM dye will not be converted to the fluorescent calcein because the intercellular esterases are absent. Thus, the dead cells simply appear as reddish-orange nuclei. We have also used calcein AM and propidium iodide dyes to stain live and dead cells following pallet release, which provides equivalent results.

### 2.6. Computational fluid dynamics modelling

The computational fluid dynamics (CFD) software OpenFOAM (OpenCFD, UK) was used to model the pallet motion through the tissue culture medium. We performed a two-dimensional simulation that solves the momentum and continuity equations describing the incompressible flow of an aqueous Newtonian fluid. The pallet and surrounding aqueous media were modelled using a two-dimensional mesh. As shown in figure 4, we used the  $Y$ – $Z$  plane as a plane of symmetry and simulated the dynamics of half a pallet element moving in the  $Z$  direction through the aqueous medium. Mesh points were assigned below the pallet, which expanded based on the pallet velocity data gathered from the interferometry measurements.

The computational domain had overall spatial dimensions of  $1.5 \times 1.5 \text{ mm}$ . These dimensions are  $30\times$  larger than the pallet itself and ensured that the motion of the pallet had negligible influence on the fluid conditions at the distal boundaries located at  $(X = 1.5 \text{ mm}, Z)$  and  $(X, Z = 1.5 \text{ mm})$ . The resolution of the computational mesh varied with distance away from the pallet. All fluid elements in contact with the pallet were meshed with a spatial resolution of  $1 \mu\text{m}$ . Moving away from the pallet surface, the mesh was gradually made coarser, reaching a spatial resolution of  $10 \mu\text{m}$  at locations distal from the pallet. This mesh allowed us to assess the hydrodynamics on the

pallet surface with 1  $\mu\text{m}$  spatial resolution. The computational domain was sufficiently large compared with the size of the pallet element such that a zero pressure gradient was applied on all boundaries for pressure excluding the top boundary, where the pressure was fixed and held constant. A no slip condition was applied to the pallet surfaces. For all other boundaries of the computational domain, a zero velocity gradient was imposed ( $\partial v/\partial x, \partial v/\partial z = 0$ ). The zero velocity gradient condition is justified because the ( $X = 1.5 \text{ mm}, Z$ ) and ( $X, Z = 1.5 \text{ mm}$ ) boundaries are far away from the pallet motion, and ( $X = 0 \text{ mm}, Z$ ) lies in the symmetry plane.

To model the fluid flow in the aqueous medium produced by the upward motion (positive  $Z$  direction) of the pallet element, we instructed the CFD simulation to move the pallet vertically in accordance with the time-resolved velocities measured by the interferometer and considered the cases corresponding to a fixed focal volume offset of  $h = 6 \mu\text{m}$  and  $E_p = 2.5, 3.0$  and  $3.5 \mu\text{J}$ . As a cross-check, we confirmed that the results provided by the CFD model matched the solution for flow normal to a flat plate, using a combination of boundary-layer and potential flow theory under steady flow conditions [33,34].

### 3. RESULTS AND DISCUSSION

#### 3.1. Release threshold at different focal heights

The pallet release probability was measured for axial focal volume heights of  $h = 2, 4, 6, 8, 10 \mu\text{m}$  by counting the number of successful release events when irradiating 20 different pallets elements each with a single-pulsed laser microbeam exposure at discrete pulse energies. This range of heights was chosen because focusing the microbeam at the glass–pallet interface ( $h = 0 \mu\text{m}$ ) or in the glass (negative  $h$  values) resulted in less consistent results and damage to the BK-7 glass support. The probability as a function of pulse energy  $p(E_p)$  was fit to a Gaussian error function of the form

$$p(E_p) = \frac{1}{2} \{1 + \text{erf}[S(E_p - E_{\text{th}})]\}, \quad (3.1)$$

where  $\text{erf}(x)$  is the error function, and  $S$  and  $E_{\text{th}}$  are fitting parameters.  $E_{\text{th}}$  denotes the pallet release energy threshold and is defined as the laser pulse energy that releases the pallet at 50 per cent probability.  $S$  denotes the sharpness of the probability curve.

The experiment data and the fit curve for three focal volume positions are shown in figure 5. Ideally, we wish to operate at the lowest possible energy that provides consistent pallet release. Thus, it is necessary to consider both the threshold and the sharpness of these probability curves. The pulse energies that provide 50 per cent (threshold) and 99 per cent release probability as well as sharpness of the fit curves are provided in table 1. The threshold pallet release energy is clearly minimized at  $h = 6 \mu\text{m}$ . Moreover, the sharpness of the Gaussian error function reaches its highest at  $h = 6 \mu\text{m}$ . This high sharpness means that only a small increase in pulse energy beyond the threshold energy results in a substantial increase in the release

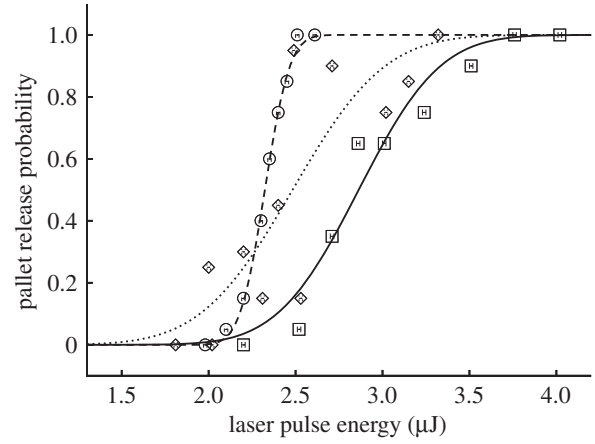


Figure 5. Pallet release probability for different focal volume positions. Squares with solid line,  $h = 2 \mu\text{m}$ ; circles with dashed line,  $h = 6 \mu\text{m}$ ; diamonds with dotted line,  $h = 10 \mu\text{m}$ .

Table 1. Pulse energies at 50% and 99% pallet release probabilities and sharpness of the release probability curves at different focal volume positions.

$h$ ( $\mu\text{m}$ )	pulse energy ( $\mu\text{J}$ ) (for 50% release)	pulse energy ( $\mu\text{J}$ ) (for 99% release)	sharpness $S$ ( $\mu\text{J}^{-1}$ )
2	2.86	3.72	1.92
4	2.49	2.96	3.49
6	2.32	2.59	6.25
8	2.44	3.06	2.67
10	2.48	3.45	1.70

probability and is responsible for the small difference between the pulse energies that achieve 50 and 99 per cent release probabilities. These experimental results establish  $h = 6 \mu\text{m}$  as the axial focal volume position that provides for consistent pallet release at the lowest microbeam pulse energy.

These results are consistent with the fact that plasmas formed using focused laser microbeam radiation are initiated at the beam waist and grow primarily in a direction counter to the propagation of the laser beam [35]. Moreover, the length of such plasmas are known to scale with the Rayleigh length of the incident laser beam [35]. Thus, for  $h = 0 \mu\text{m}$ , the bulk of the plasma is located in the glass support and thus not effective for efficient pallet release. For a numerical aperture of 0.45 at  $\lambda = 532 \text{ nm}$ , the Rayleigh length of the pulsed laser microbeam is approximately  $3 \mu\text{m}$ , roughly  $3\times$  smaller than the location of the beam waist  $h' = n_p h \approx 10 \mu\text{m}$  from the pallet–glass interface when optimal pallet release is achieved. It is believed that the focal volume position of  $h = 6 \mu\text{m}$  provides for plasma-mediated ablation of a sufficient amount of polymer at a location proximal enough to the pallet–glass interface for the ablation products to disrupt the interface and provide for efficient pallet release.

#### 3.2. Pallet release dynamics

While the pallet release process has been imaged with nanosecond time resolution and reveals events

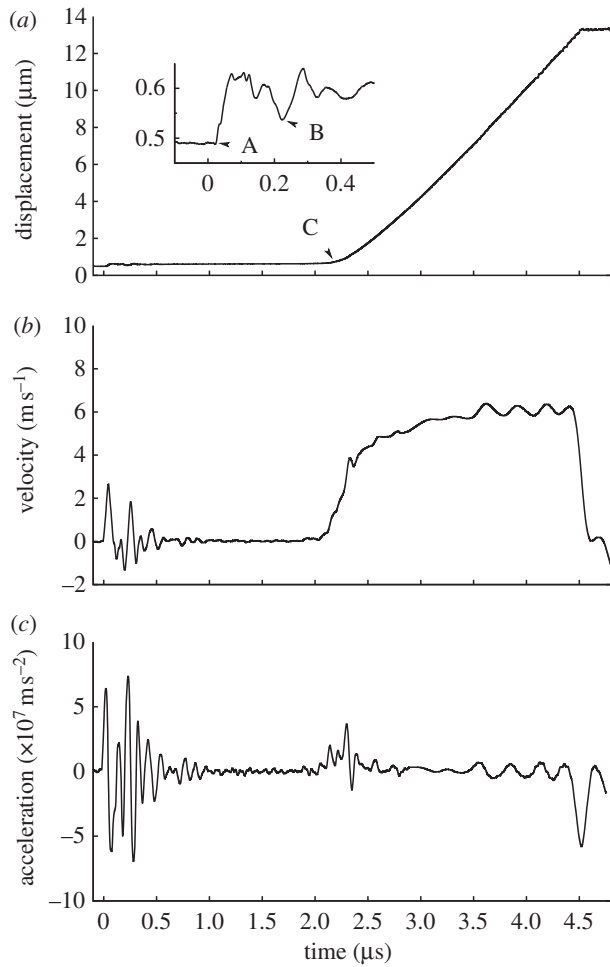


Figure 6. Representative pallet (a) displacement, (b) velocity and (c) acceleration for  $E_p = 3.5 \mu\text{J}$  and  $h = 6 \mu\text{m}$  obtained from the interferometry data. (a) A denotes the initial upward pallet motion owing to the plasma-induced shock wave, B denotes either permanent deformation of the pallet or elastic recoil owing to the initial shock wave excitation and C denotes the initiation of the pallet release. The breakdown of these traces at times larger than approximately  $4.5 \mu\text{s}$  is from the loss of the interferometer signal owing to rotational motion of the pallet.

occurring on nanosecond and microsecond time-scales [15], no quantitative measurements of the pallet velocities have been performed to date. In this study, we used a time-resolved interferometer technique to provide the first quantitative measurements of pallet release dynamics following pulsed laser microbeam irradiation for focal volume heights of  $h = 2, 6, 10 \mu\text{m}$  and pulse energies  $E_p = 2.5, 3.0, 3.5 \mu\text{J}$ . We performed six pallet release trials for each combination of focal volume height and pulse energy. As noted later, in some trials, the pulse energy used did not provide 100 per cent release probability and resulted in pallets that were remained adherent or only partially released. The interferometer data from partially released pallets are not usable owing to rapid signal loss from pallet tilting. Data from pallets that remained adherent or were only partially released were excluded from the results and analysis. A representative trial for a pallet released using  $h = 6 \mu\text{m}$  and  $E_p = 3.5 \mu\text{J}$  is shown in figure 6.

Figure 6a contains a wealth of data regarding the dynamics of the pallet release process. First, we observe a clear upward displacement of the sample surface at  $t_A \sim 20 \text{ ns}$  (point A) following the laser microbeam exposure at  $t = 0$ . This feature is nearly independent of both laser microbeam pulse energy and focal volume height and observed even in cases when the pallet is not subsequently released. This feature is likely generated by the shock wave produced by the optical breakdown near the interface between the pallet and the glass substrate. Another consistent feature in the signal appears near  $t_B = 220 \text{ ns}$  (point B) and is also independent of the laser pulse energy, focal volume height and subsequent pallet release. This feature may be due to an elastic rebound of the pallet surface induced by the shock wave passage and/or permanent deformation of the pallet through plasma-mediated ablation of the polymer, the latter of which has been corroborated by time-resolved photography [15]. In this trial, pallet release occurs near  $t_C = 2.1 \mu\text{s}$  (point C). Time-resolved photography indicates that this delay is connected with the time required for the gaseous products of the plasma-mediated ablation to fully disrupt the adhesion between the polymer pallet and the underlying glass [15]. Once the interface is fully disrupted, the high pressure of the gas is able to accelerate the pallet upward. Once released, the pallet accelerates rapidly over the next approximately 300 ns after which it reaches a constant velocity approaching  $6 \text{ m s}^{-1}$ . At  $t = 4.5 \mu\text{s}$ , the interferometer signal is lost owing to the rotational movement of the released pallet. This sequence of events starting with shock-wave emission, permanent pallet deformation, pallet release and pallet rotation is fully consistent with the sequence of events visualized via time-resolved imaging of the pallet release process [15].

The release time  $t_C$  depends on the focal volume height and the laser pulse energy. Even for a fixed focal position and pulse energy, we sometimes see a significant variation in the pallet release time  $t_C$  with standard deviations that always exceed 500 ns and well in excess of the 3 ns temporal resolution of the interferometer. The release time as a function of focal volume height and pulse energy is plotted in figure 7a. The figure generally shows a reduction in the pallet release time with increases in either the microbeam pulse energy or the axial focal volume position over the parameter range examined. Note that while the pallet release probability for  $h = 6 \mu\text{m}$  is nearly 100 per cent for each of these three pulse energies, for  $h = 2 \mu\text{m}$ , the release probabilities are 16, 65 and 96 per cent at pulse energies of  $E_p = 2.5, 3.0$  and  $3.5 \mu\text{J}$ , respectively, while for  $h = 10 \mu\text{m}$ , these release probabilities are 52, 89 and 99 per cent. No reliable results are available for  $E_p = 2.5 \mu\text{J}$  at  $h = 2 \mu\text{m}$  owing to the low release probability, which also leads to very inconsistent data. The maximum velocity and the maximum acceleration are shown in figure 7b,c, respectively. The maximum velocity generally increases with both laser microbeam pulse energy and focal volume position over the parameter range examined.

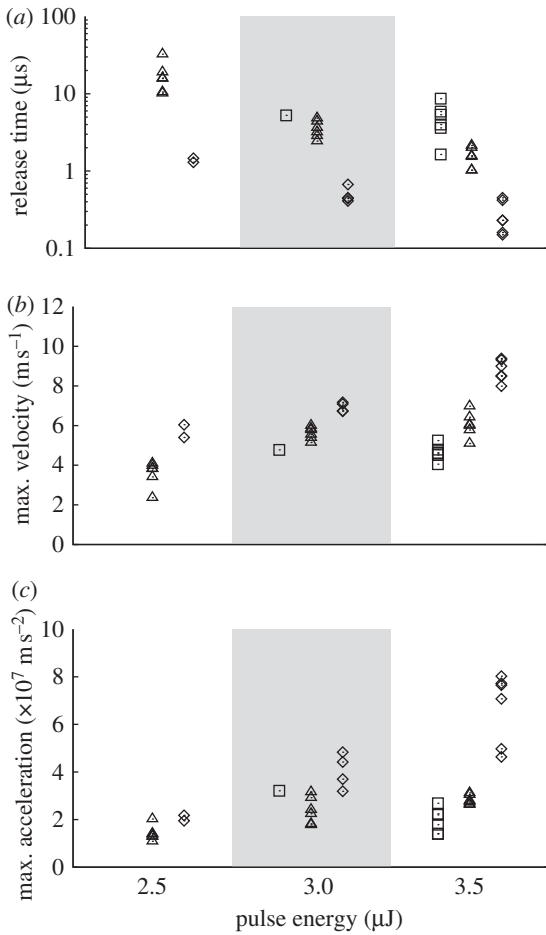


Figure 7. Release time, maximum release velocity and maximum release acceleration as a function of microbeam pulse energy and focal volume position. Squares,  $h = 2 \mu\text{m}$ ; triangles,  $h = 6 \mu\text{m}$ ; diamonds,  $h = 10 \mu\text{m}$ .

### 3.3. Cell viability

Figure 8 provides images of the confluent pallets with HeLa cells before and after release into the adjoining dish. We limited our experiments to an axial focal volume location of  $h = 6 \mu\text{m}$  and examined the cell viability at three microbeam pulse energies  $E_p = 2.5, 3.0$  and  $3.5 \mu\text{J}$ . At each pulse energy, we released and recovered a minimum of 20 pallets. We found a distinct drop in overall cell viability with increase in pulse energy. Specifically, pulse energies of  $E_p = 2.5, 3.0$  and  $3.5 \mu\text{J}$  resulted in cell viability rates of 91 per cent, 72 per cent and 66 per cent, respectively. However, a closer examination revealed that the locations of the dead cells on these pallets were not randomly distributed. Rather, cells situated on the pallet periphery were more susceptible to necrosis following release when compared with cells situated at the pallet centre, which always remained viable.

This observation prompted us to map the location of the cells relative to the centre of the pallet. Because all the four quadrants of the square pallet are equivalent, we reassigned the location of cells residing in the second through fourth quadrants to the equivalent location in the first quadrant. In figure 9, we provide the viability statistics as a function of cell location on the pallet for all three pulse energies  $E_p = 2.5, 3.0$  and

$3.5 \mu\text{J}$  at  $h = 6 \mu\text{m}$ . In this figure, the lower left-hand corner represents the centre of the pallet and the  $x$  and  $y$  axes represent the horizontal and vertical mid-lines of the pallet. The top and right-hand edges represent the pallet periphery. Figure 9 shows a strong correlation between cell location and its subsequent viability following pallet release. For  $E_p = 2.5 \mu\text{J}$ , we see that cells located within  $\lesssim 40 \mu\text{m}$  of the pallet centre experience viability rates greater than 90 per cent, with cells residing within  $10 \mu\text{m}$  from the pallet edge experiencing a reduced viability rate of 84 per cent. For higher pulse energies of  $E_p = 3.0$  and  $3.5 \mu\text{J}$ , the news is less promising. Cells located within  $30 \mu\text{m}$  of the pallet centre experience viability rates greater than 85 per cent, while cells residing greater than  $30 \mu\text{m}$  from the pallet centre are much more susceptible to necrosis with cell viability in the range 40–70%. These viability rates are compared directly in figure 10. These data strongly indicate that the spatial variation in cell viability is not linked to global velocities or accelerations of the entire pallet. This is because while all the cells on a given pallet element experience the same pallet velocities and accelerations, they have very different susceptibilities to cell death based on their spatial position on the pallet surface as shown in figures 9 and 10. Moreover, even at the highest pulse energies, which result in the highest velocities and acceleration, the cells closest to the pallet centre retain 100 per cent viability. This demonstrates that the global velocities and/or acceleration by themselves are not responsible for the observed cell death. Rather, cell death is linked to factors that have a disproportionate impact on cells positioned on the pallet periphery that increases in severity with increases in pulse energy.

### 3.4. Shear stresses predicted from computational fluid dynamics simulation

In figure 11, we provide (i) the time-resolved pallet velocity profiles that we obtained from our interferometry measurements for  $h = 6 \mu\text{m}$  and supplied to the OpenFOAM CFD model for the three pulse energies and (ii) the resulting time-resolved shear stress predicted by the OpenFOAM CFD model for  $E_p = 3.0 \mu\text{J}$  at various locations on the pallet surface where  $x = 0$  denotes the pallet centre and  $x = 50 \mu\text{m}$  denotes the pallet edge. In figure 11a, we provide as input the pallet velocity profiles in the neighbourhood of the pallet release because the early nanoscopic motions that appear immediately after laser irradiation and the length of the delay time prior to pallet release (shown in figure 6) have a negligible impact on the resulting shear stresses. The shear stresses shown in figure 11b correspond to the velocities generated by pallet release with a pulse energy of  $3.0 \mu\text{J}$  and a focal volume location of  $h = 6 \mu\text{m}$ . The shear stress at the centre of the pallet is zero because the flow is symmetric about this location. The time-resolved shear stress profiles show that positions towards the periphery of the pallet experience much larger shear stresses. To make this latter point clearer, in figure 12, we plot the maximum shear stress as a function of pallet location for an axial focal volume position of  $h = 6 \mu\text{m}$  at pulse

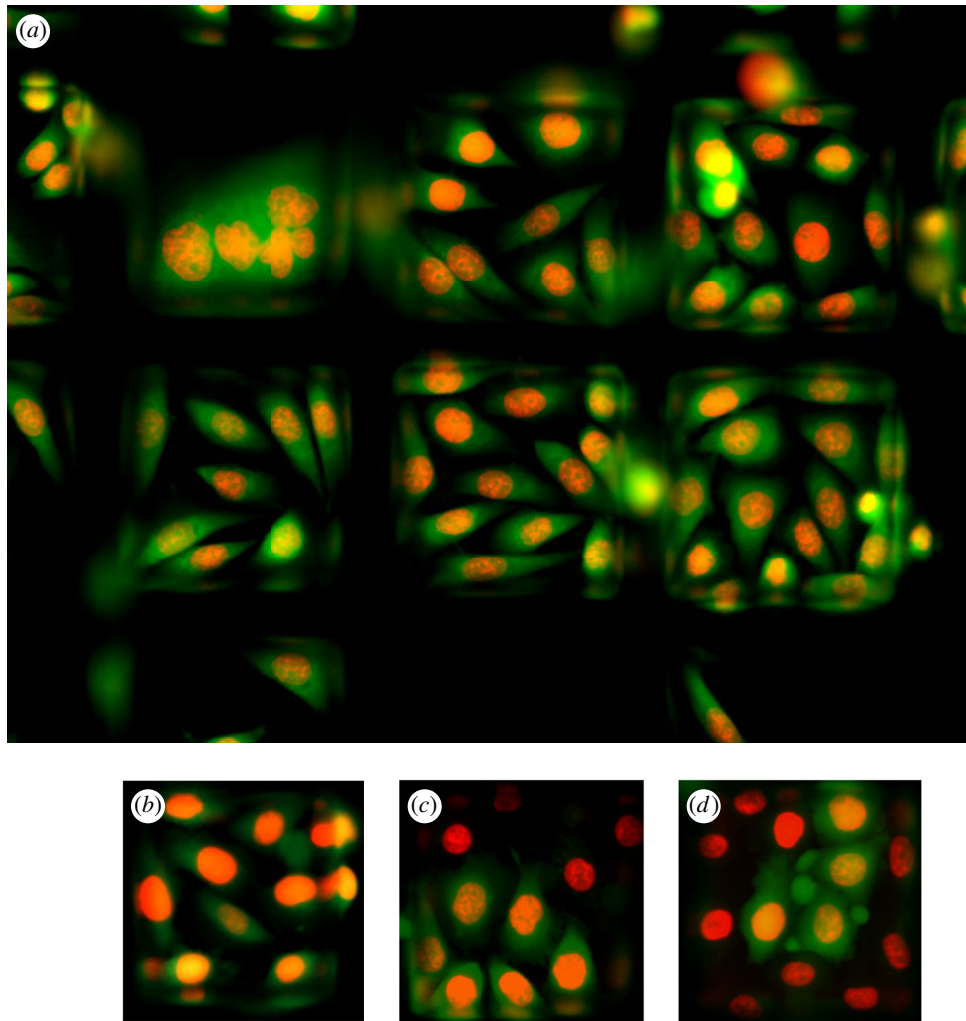


Figure 8. (a) Co-stained calcein AM (green) and Hoechst 33342 (red) confluent HeLa cells on pallets prior to release; (b–d) pallets after release using pulse energies of (b)  $2.5 \mu\text{J}$ , (c)  $3.0 \mu\text{J}$  and (d)  $3.5 \mu\text{J}$ . Axial position of focal volume was  $h = 6 \mu\text{m}$ . As described in the text, live cells will possess a green cytoplasm with an orange nucleus while dead cells will appear with only a red nucleus without any green staining.

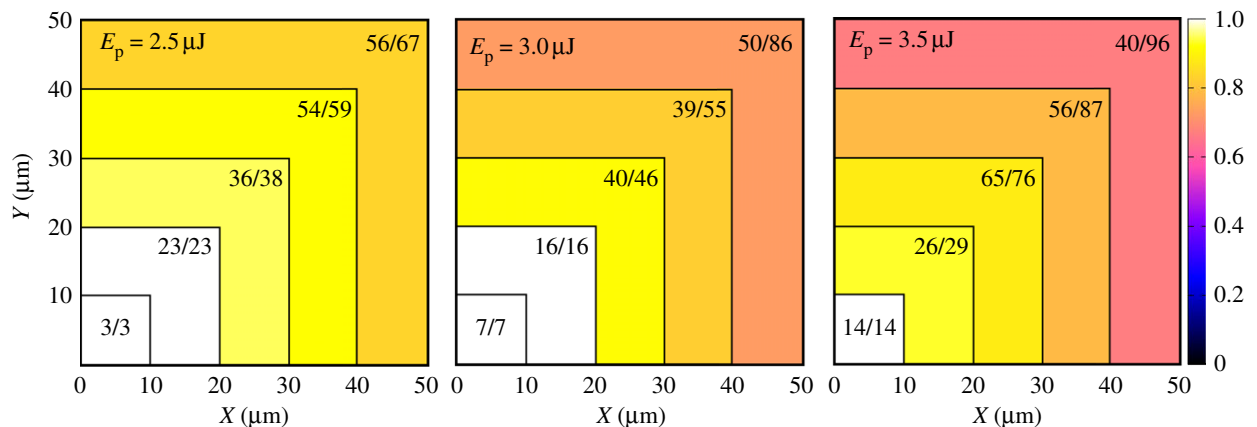


Figure 9. Graphical depiction of variation in cell viability rates on the pallet surface as a function of pulse energy. MM/NN refers to the number of viable cells counted out of the total number of cells residing in the respective regions.

energies of 2.5, 3.0 and  $3.5 \mu\text{J}$ . Overall, we see the presence of significantly larger shear stresses with increases in laser microbeam energy. By cross-referencing the maximum shear stress values shown in figure 12 with the viability results shown in figure 10, we find that locations on the pallet that experience maximum shear

stress values of  $\tau_{\text{max}} \lesssim 20 \text{ kPa}$  result in cell viability rates of greater than 90 per cent and that larger shear stresses produce significant reductions in cell viability. The correlation between cellular exposure to microsecond duration impulses of shear stress exceeding 20 kPa and subsequent cell death is consistent with other studies

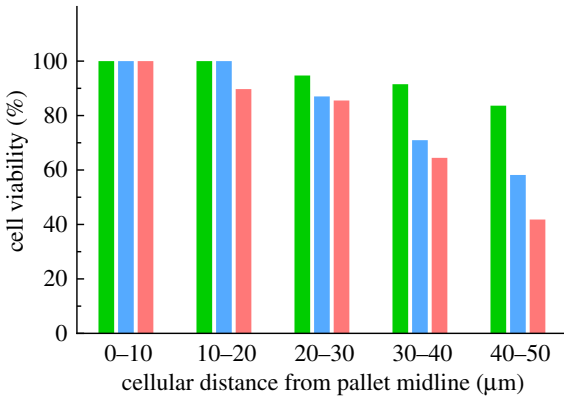


Figure 10. Variation in cell viability rates with pulse energy and cellular position on the pallet surface. Increases in pulse energy and/or cell position away from the pallet centre will increase cellular exposure to hydrodynamic shear stress during release and reduces cell viability. Green bars, 2.5  $\mu\text{J}$ ; blue bars, 3.0  $\mu\text{J}$ ; pink bars, 3.5  $\mu\text{J}$ .

where laser-generated cavitation bubbles are used for cell lysis and drug delivery [21]. However, we should emphasize that the two-dimensional hydrodynamic model shown here will tend to overestimate the actual shear stresses present in the real three-dimensional system.

### 3.5. Comparison of pallet release to laser microdissection and laser pressure catapulting

It is interesting to examine the characteristics of this polymer micropallet technique vis-a-vis the LMD/LPC method for the isolation and selection of live cells. An earlier study by Horneffer *et al.* [6] examined the dynamics of the live-cell catapulting of 100  $\mu\text{m}$  diameter cellular samples (Chinese hamster ovary cells) achieved by the delivery of 3 ns duration  $\text{N}_2$  laser pulses at  $\lambda = 337$  nm with a pulse energy of 12  $\mu\text{J}$  delivered to the target with a 0.5 numerical aperture [6]. The authors provided astonishing detail regarding the catapulting dynamics through the use of time-resolved photography and reported on the ability to recultivate cells from the catapulted sample. However, the study did not provide direct measurements of the initial sample velocities or the resulting cell viability, which prevents the direct comparison of these results with the experimental results presented here. Nevertheless, a few features of the catapulting dynamics are worth noting. In the Horneffer study, thin (10–100  $\mu\text{m}$ ) layers of aqueous media are present both below the polymer foil that supports the cells and above the cells to maintain hydration. This multi-layered geometry complicates the physics of the release and catapulting process significantly and it is most difficult to quantitatively model the cellular exposure to the hydrodynamic and aerodynamic stresses.

Nevertheless, it is important to note that in LMD/LPC, the targets that are catapulted have been dissected and, unlike the pallets, are not adherent to a substrate. This difference affects significantly the plasma expansion, and thus, the transfer of momentum

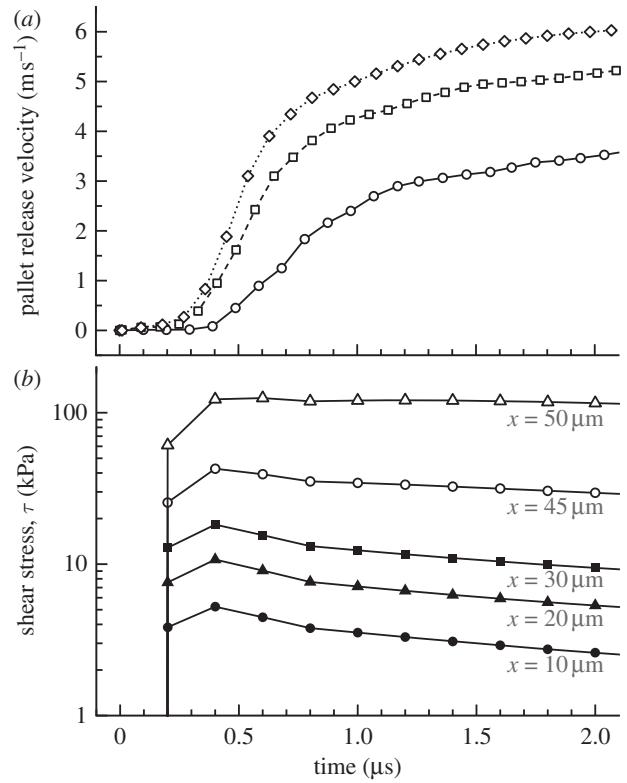


Figure 11. (a) Measured pallet release velocities for  $E_p = 2.5, 3.0$  and  $3.5 \mu\text{J}$  at focal volume position  $h = 6 \mu\text{m}$ . Diamonds with dotted line,  $E_p = 3.5 \mu\text{J}$ ; squares with dashed lines,  $E_p = 3.0 \mu\text{J}$ ; circles with solid line,  $E_p = 2.5 \mu\text{J}$ . (b) Predicted time-resolved shear-stress distributions for  $E_p = 3.5 \mu\text{J}$  and focal volume position  $h = 6 \mu\text{m}$  at various pallet surface locations.

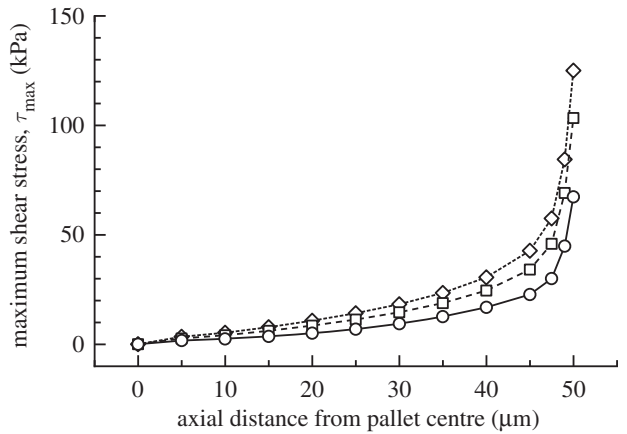


Figure 12. Spatial distributions of maximum shear stress for pulse energies of  $E_p = 2.5, 3.0$  and  $3.5 \mu\text{J}$  at focal volume position  $h = 6 \mu\text{m}$ . Diamonds with dotted line,  $E_p = 3.5 \mu\text{J}$ ; squares with dashed lines,  $E_p = 3.0 \mu\text{J}$ ; circles with solid line,  $E_p = 2.5 \mu\text{J}$ .

from the plasma to the target. More specifically, the plasma formation in LMD/LPC likely transfers more momentum to the target than in the pallet technique. This is because a portion of the energy associated with the plasma expansion is dissipated in the disruption of the adhesion at the glass–pallet interface. Moreover, the plasma expansion accelerates not only

the target but also the surrounding fluid. In LMD/LPC, the target is surrounded primarily by air and only a thin layer of water while the pallets are fully immersed in an aqueous environment. This results in initial velocities in LPC that are roughly an order of magnitude larger than those in the pallet release process. Finally, a simple calculation shows that in both techniques, the weight of the released target is more than five orders of magnitude smaller than the aerodynamic and hydrodynamic drag forces ( $\approx \frac{1}{2}\rho v^2 A$ ) imposed on a released target with surface area  $A$  and release velocity  $v$  by the surrounding air or aqueous media with density  $\rho$ . Thus, the weight of the pallet/foil is an insignificant factor in determining the release dynamics. By contrast, the drag force does limit the maximum release velocities of the samples, which, combined with the fluid viscosity of the surrounding environment, are the principal factors affecting the cellular exposure to shear stress.

When using focused pulses in LMD/LPC, the Horneffer study estimated the initial sample velocity to be  $100 \text{ m s}^{-1}$  while the use of defocused pulses reduced this velocity to  $50 \text{ m s}^{-1}$ . Moreover, the defocused pulses were delivered to the centre of the cellular sample, while focused pulses were directed on the sample periphery. This latter case resulted in the transfer of both linear and angular momentum to the cellular sample. The transfer of angular momentum resulted in significant rotation of the target exceeding  $10^5$  revolutions per second. The sample rotation reduced the tangential flow across the cellular sample, presumably reducing somewhat the cellular exposure to fluid shear. As a result, the measured recultivation efficiency for the recovered specimens released using focused pulses was 98 per cent. By contrast, the release using defocused pulses resulted in the shearing of the majority of the cells off of the underlying polymer foil and resulted in a dismal 7 per cent recultivation efficiency.

Thus, both our study and that of Horneffer and co-workers demonstrate that release strategies which reduce the cellular exposure hydrodynamic shear stresses result in higher cell viability/recultivation rates. One approach demonstrated by the Horneffer study is to irradiate the sample on its periphery, thereby imparting angular momentum and inducing sample rotation. We have explored this approach within the pallet-release context. We find that pallet release using irradiation at peripheral pallet locations requires higher pulse energies and is less consistent. A more attractive alternate strategy would be to use surface chemistry to selectively modify the periphery of the pallet elements so as to prevent cellular attachment. In this way, cells would not reside on the peripheral pallet locations that experience high levels of fluid shear during release. An even simpler approach to reducing cellular exposure to hydrodynamic shear stresses is to create three-dimensional pallet elements that allow the cells to be cultured on indented, rather than on planar, surfaces. Such ‘microcup arrays’ [18], developed by the Allbritton group, ensure that a static layer of fluid is present above the cells but within the microcup. This displaces the cells vertically from the fluid boundary layer that forms during the pallet release process

and effectively insulates them from the hydrodynamic shear stresses.

#### 4. SUMMARY AND CONCLUSIONS

We have examined the impact of laser microbeam energy and focal volume position parameters on the release dynamics of 1002F photoresist polymer micropallets and subsequent cell viability. We show that the position of the microbeam focal volume relative to the glass–pallet interface is critical to achieve consistent pallet release and minimize the pallet release velocity. Moreover, once the microbeam focal volume position is optimized, we show the importance of using the lowest possible pulse energy that guarantees pallet release so as to minimize the release velocity. We demonstrate through hydrodynamic modelling that increases in pulse energy, and thereby pallet release velocity, can increase the cellular exposure to transient hydrodynamic shear stresses to  $\gtrsim 100 \text{ kPa}$  on microsecond timescales resulting in reduced cell viability. Moreover, the hydrodynamic modelling revealed the highly non-uniform spatial distribution of shear stresses on the pallet surface with the largest shear stresses occurring on the pallet periphery. The experiments that examine cell viability of confluent cell cultures on the pallet surface confirm that when releasing pallets using larger pulse energies, increases in a given cell position from the pallet centre increases its susceptibility to necrosis. Nevertheless, cell viability experiments that examine the release of confluent cell cultures reveal that when appropriate pulse energies are used, cell viability rates of approximately greater than 90 per cent can be achieved and correspond to the exposure of transient hydrodynamic shear stresses approximately less than  $20 \text{ kPa}$ .

We thank Ben Colcord for his assistance with the CFD simulations. We acknowledge support from the National Institutes of Health (NIH) via R01 HG004843 and R43 RR025980. We also acknowledge the support of the Laser Microbeam and Medical Programme, an NIH Biomedical Technology Resource via P41-RR01192. M.R. and D.W.S. are involved in the commercial development of the iCell pallet release apparatus. All experiments and data analysis were performed by UC Irvine researchers who have no conflict of interest.

#### REFERENCES

- 1 Patel, D. 2001 *Separating cells*. New York, NY: Springer.
- 2 Welm, B., Behbod, F., Goodell, M. A. & Rosen, J. M. 2003 Isolation and characterization of functional mammary gland stem cells. *Cell Prolif.* **36**, 17–32. (doi:10.1046/j.1365-2184.36.s.1.3.x)
- 3 Seidl, J., Knuechel, R. & Kunz-Schughart, L. A. 1999 Evaluation of membrane physiology following fluorescence activated or magnetic cell separation. *Cytometry* **36**, 102–111. (doi:10.1002/(SICI)1097-0320(19990601)36:2<102::AID-CYTO3>3.0.CO;2-D)
- 4 Schutze, K. & Lahr, G. 1998 Identification of expressed genes by laser-mediated manipulation of single cells. *Nat. Biotechnol.* **16**, 737–742. (doi:10.1038/nbt0898-737)
- 5 Schutze, K., Posl, H. & Lahr, G. 1998 Laser micromanipulation systems as universal tools in cellular and molecular biology and in medicine. *Cell Mol. Biol.* **44**, 735–746.

- 6 Horneffer, V., Linz, N. & Vogel, A. 2007 Principles of laser-induced separation and transport of living cells. *J. Biomed. Opt.* **12**, 054016. (doi:10.1117/1.2799194)
- 7 Vogel, A., Lorenz, K., Horneffer, V., Hüttmann, G., von Smolinski, D. & Gebert, A. 2007 Mechanisms of laser-induced dissection and transport of histologic specimens. *Biophys. J.* **93**, 4481–4500. (doi:10.1529/biophysj.106.102277)
- 8 Vogel, A., Horneffer, V., Lorenz, K., Linz, N., Hüttmann, G. & Gebert, A. 2007 Principles of laser microdissection and catapulting of histologic specimens and live cells. In *Laser manipulation of cells and tissues. Methods in cell biology*, vol. 82 (eds. M. W. Berns & K. O. Greulich), pp. 153–205. New York, NY: Academic Press.
- 9 Burgemeister, R. 2005 New aspects of laser microdissection in research and routine. *J. Histochem. Cytochem.* **53**, 409–412. (doi:10.1369/jhc.4B6421.2005)
- 10 Espina, V., Wulfkühle, J. D., Calvert, V. S., VanMeter, A., Zhou, W., Coukos, G., Geho, D. H., Petricoin III, E. F. & Liotta, L. A. 2006 Laser-capture microdissection. *Nat. Protoc.* **1**, 586–603. (doi:10.1038/nprot.2006.85)
- 11 Salazar, G. T., Wang, Y., Young, G., Bachman, M., Sims, C. E., Li, G. P. & Allbritton, N. L. 2007 Micropallet arrays for the separation of single, adherent cells. *Anal. Chem.* **79**, 682–687. (doi:10.1021/ac0615706)
- 12 Wang, Y., Young, G., Bachman, M., Sims, C. E., Li, G. P. & Allbritton, N. L. 2007 Collection and expansion of single cells and colonies released from a micropallet array. *Anal. Chem.* **79**, 2359–2366. (doi:10.1021/ac062180m)
- 13 Salazar, G. T., Wang, Y., Sims, C. E., Bachman, M., Li, G. P. & Allbritton, N. L. 2008 Characterization of the laser-based release of micropallets from arrays. *J. Biomed. Opt.* **13**, 034007. (doi:10.1117/1.2937475)
- 14 Pai, J.-H., Wang, Y., Salazar, G. T., Sims, C. E., Bachman, M., Li, G. P. & Allbritton, N. L. 2007 Photoresist with low fluorescence for bioanalytical applications. *Anal. Chem.* **79**, 8774–8780. (doi:10.1021/ac071528q)
- 15 Quinto-Su, P. A., Salazar, G. T., Sims, C. E., Allbritton, N. L. & Venugopalan, V. 2008 Mechanisms of pulsed laser microbeam release of SU-8 polymer ‘micropallets’ for the collection and separation of adherent cells. *Anal. Chem.* **80**, 4675–4679. (doi:10.1021/ac800129a)
- 16 Wang, Y., Young, G., Pai, J.-H., Aoto, P. C., Bachman, M., Li, G. P., Sims, C. E. & Allbritton, N. L. 2007 Broadening cell selection criteria with micropallet arrays of adherent cells. *Cytometry* **71A**, 866–874. (doi:10.1002/cyto.a.20424)
- 17 Shadpour, H., Sims, C. E., Thresher, R. J. & Allbritton, N. L. 2009 Sorting and expansion of murine embryonic stem cell colonies using micropallet arrays. *Cytometry* **75A**, 121–129. (doi:10.1002/cyto.a.20672)
- 18 Xu, W., Sims, C. E. & Allbritton, N. L. 2010 Microcup arrays for the efficient isolation and cloning of cells. *Anal. Chem.* **82**, 3161–3167. (doi:10.1021/ac100434v)
- 19 Rau, K. R., Guerra III, A. G., Vogel, A. & Venugopalan, V. 2004 Investigation of laser-induced cell lysis using time-resolved imaging. *Appl. Phys. Lett.* **84**, 2940–2942. (doi:10.1063/1.1705728)
- 20 Rau, K. R., Quinto-Su, P. A., Hellman, A. N. & Venugopalan, V. 2006 Pulsed laser microbeam-induced cell lysis: time-resolved imaging and analysis of hydrodynamic effects. *Biophys. J.* **91**, 317–329. (doi:10.1529/biophysj.105.079921)
- 21 Hellman, A. N., Rau, K. R., Yoon, H. H. & Venugopalan, V. 2008 Biophysical response to pulsed laser microbeam-induced cell lysis and molecular delivery. *J. Biophotonics* **1**, 24–35. (doi:10.1002/jbio.200710010)
- 22 Ohl, C.-D., Arora, M., Ikink, R., Versluis, M., de Jong, N., Delius, M. & Lohse, D. 2006 Sonoporation from jetting cavitation bubbles. *Biophys. J.* **91**, 4285–4295. (doi:10.1529/biophysj.105.075366)
- 23 Dijkink, R., Le Gac, S., Nijhuis, E., van den Berg, A., Vermes, I., Poot, A. & Ohl, C.-D. 2008 Controlled cavitation–cell interaction: trans-membrane transport and viability studies. *Phys. Med. Biol.* **53**, 375–390. (doi:10.1088/0031-9155/53/2/006)
- 24 Wang, Y., Phillips, C., Xu, W., Pai, J.-H., Dhopeswarkar, R., Sims, C. E. & Allbritton, N. 2010 Micromolded arrays for separation of adherent cells. *Lab Chip* **10**, 2917–2924. (doi:10.1039/c0lc00186d)
- 25 Carp, S. A. & Venugopalan, V. 2007 Optoacoustic imaging based on the interferometric measurement of surface displacement. *J. Biomed. Opt.* **12**, 064001. (doi:10.1117/1.2812665)
- 26 Carp, S. A., Guerra III, A., Duque Jr, S. Q. & Venugopalan, V. 2004 Optoacoustic imaging using interferometric measurement of surface displacement. *Appl. Phys. Lett.* **85**, 5772–5774. (doi:10.1063/1.1831569)
- 27 Payne, B. P., Venugopalan, V., Mikić, B. B. & Nishioka, N. S. 2003 Optoacoustic tomography using time-resolved interferometric detection of surface displacement. *J. Biomed. Opt.* **8**, 273–280. (doi:10.1117/1.1559727)
- 28 Yablon, A. D., Nishioka, N. S., Mikić, B. B. & Venugopalan, V. 1999 Measurement of tissue absorption coefficients by use of interferometric photothermal spectroscopy. *Appl. Opt.* **38**, 1259–1272. (doi:10.1364/AO.38.001259)
- 29 Abbas, G. L., Chan, V. W. S. & Yee, T. K. 1983 Local-oscillator excess-noise suppression for homodyne and heterodyne detection. *Opt. Lett.* **8**, 419–421. (doi:10.1364/OL.8.000419)
- 30 Marti, O., Holzwarth, M. & Beil, M. 2008 Measuring the nanomechanical properties of cancer cells by digital pulsed force mode imaging. *Nanotechnology* **19**, 384015. (doi:10.1088/0957-4484/19/38/384015)
- 31 Marmur, A. 2003. Wetting on hydrophobic rough surfaces: to be heterogeneous or not to be? *Langmuir* **19**, 8343–8348. (doi:10.1021/la0344682)
- 32 Ras, M. 2010 The technology behind understanding cells and diseases. *Med. Des.* **10**, 29–31.
- 33 Schlichting, H. 1979 *Boundary-layer theory*, 7th edn. New York, NY: McGraw-Hill.
- 34 White, F. M. 2011 *Fluid mechanics*, 7th edn. New York, NY: McGraw-Hill.
- 35 Vogel, A., Nahen, K., Theisen, D. & Noack, J. 1996 Plasma formation in water by picosecond and nanosecond Nd:YAG laser pulses. I. Optical breakdown at threshold and superthreshold irradiance. *IEEE J. Select. Top. Quant. Electron.* **2**, 847–860. (doi:10.1109/2944.577307)